

Scaling Dynamic Failure: A Numerical Study

T. Noam, M. Dolinski and D. Rittel*

Faculty of Mechanical Engineering, Technion, 32000 Haifa, Israel

Abstract

Scaling failure in blast loaded structures is considered to be impossible with the known scaling laws when using fracture mechanics-based (fracture toughness) considerations (Jones, 1989). We will show in this research that scaling failure becomes possible when 2 alternative competing criteria are used, namely: *maximum normal stress* to describe separation (cracking) and a *strain energy density-based criterion* that describes adiabatic shear failure. Numerical simulations of two test-cases were carried out: Failure of circular clamped plates under close-range, air blast loading, and penetration experiments.

This study shows that both the prototype and small-scale model undergo scaling for those failure criteria. This study presents a new alternative to the scaling of structural failure under dynamic loading conditions, which is both simple and efficient.

Keywords: Adiabatic Shear, Scaling, Dynamic Failure, Strain Energy Density, Blast, Penetration

(*) **Corresponding author:** merittel@technion.ac.il

1. Introduction

From an engineering perspective, the usage of small-scale models can be very effective, as it saves both time and expensive full-scale experiments. By using a small-scale model, one could greatly decrease the difficulty of setting up an experiment, which aside from financial considerations, might also be hazardous (violent blast for instance).

Scaling structural failure in dynamic problems is considered to be impossible while using the established scaling laws if one assumes use of a fracture mechanics criteria [1]. In order to successfully scale a prototype (full-scale), one must make sure that both the geometry of the model (small-scale) and the failure mechanism used for the model follow the scaling laws. It is discussed in section 2 that this is not possible for a fracture mechanics-based (fracture toughness) criterion. Scaling a dynamic failure problem therefore requires an alternative failure mechanism that is not based on fracture mechanics. Adiabatic shear banding (ASB) is one of the many failure mechanisms that occur in dynamic (high strain-rate) loading situations. The homogeneous deformation tends to localize into a narrow band (ASB) followed by catastrophic failure [2]. The typical time scale involved is short, so that one can consider this failure mechanism as adiabatic, with large associated temperature increases, especially inside the band. Many materials fail by adiabatic shear banding in an uncontrolled and dangerous manner [2][2][3]. One failure criterion, proposed by Rittel et al. [4], is described by

$$E = \int_0^{\varepsilon_f} \sigma_{ij} d\varepsilon_{ij}^p \quad (1)$$

Where σ and ε are the stress and strain tensors. Such a criterion may remind of the work by Cockcroft and Latham [5], albeit in the specifically dynamic context. However, the major difference is that it is developed within a physical context (driven from microstructural considerations) and specifically applied to the dynamic case.

The strain energy density criterion (critical value of E in eqn (1)) is based on the dynamic deformation energy of cold work, and suggests that the dynamic deformation energy is the governing factor governing ASB formation. In

experiments conducted by Rittel et al. [4], it was shown that this energy was constant irrespective of static pre-strain levels before dynamic failure, or interruptions in a dynamic test that minimized thermomechanical coupling effects. According to the criterion, a material point starts to fail when the total strain energy density reaches a critical value, the latter being measurable, and different for each material.

Other known (static or dynamic) failure mechanisms include Gurson's model [6], Grady's fragmentation model [7], and the true ductility criterion by Cockcroft and Latham [5]. Gurson's model is based on the plastic flow of a material that contains voids. This model is complex, and requires a number of constants and conditions that one must determine to use this model. An example of a damage criterion, based on a modified version of Gurson's model, can be found in the work of Longère et al. [8]. In the author's words [7], "Grady considered improvements to two aspects of the Mott model of fragmentation [9]: the instantaneous appearance of the fracture and the inability to pin down the statistical properties of the failure strain in the material". Mott's model considers statistical aspects such as standard deviation in fracture strains, that can't necessarily be measured in independent experiments. Grady's model involves a large number of parameters that must be known in order to estimate the failure strain. Although Grady's model has been validated [10], we have not found (widespread) engineering applications of this failure model. The Cockcroft and Latham true ductility criterion [5] for a material is the strain at fracture in an idealized test, in which the stress is always of uniaxial tension. This criterion does not directly correlate to an energy based criterion, except for ideally plastic materials. Moreover, this criterion is proposed for the static failure case, although sometimes employed in dynamic situations [11]. All of these failure criteria may undergo scaling under certain conditions, but we have not found any mention of scaled applications, or considerations based on these criteria.

In order to fully understand the blast mechanism, we first need to understand the nature of a blast wave. A blast wave is basically a pressure wave, resulting from the release of a large amount of energy, in a small and very

localized volume. In our case we discuss only a spherical air burst for simplicity.

The pressure at each and every point is a function of the distance from the explosion point and the strength of the explosion. When checking the effect of a blast on a plate or structure of any sort, it is assumed that only the positive phase be taken into account, as the negative phase can be neglected compared to it. The pressure applied to the plate is [12]:

$$\begin{cases} P_{eff}(t) = P_{inc}(t) \cdot [1 + \cos^2 \theta - 2 \cos \theta] + P_{ref}(t) \cdot \cos^2 \theta, & \cos \theta \geq 0 \\ P_{eff}(t) = P_{inc}(t) & \cos \theta < 0 \end{cases} \quad (2)$$

where the angle of incidence θ is formed by the line from the charge center to the point of interest on the structure and the normal vector of the structure's surface at that point, P_{eff} is the effective pressure applied to the plate, P_{inc} is the incident pressure, and P_{ref} is the reflected pressure.

2. Scaling Theory

When using scaling theory to compare between a full-scale *prototype* and small-scale *model*, there are relationships between the parameters of the prototype and the small-scale model that must be fulfilled, as discussed e.g. in Jones [1].

This author mentions two important points of the scaling theory. The first concerns geometrically similar scaling, as applied only to linear elastic solids. The second consists of the Buckingham Π -theorem, which also applies to dynamic cases with inelastic response, being, as such, relevant to this work. The scaling laws remain the same for both subjects, thus they can be used for both elastic and inelastic responses. We will present only the relevant parameters for our problem, where a lower case letter represents the small-scale model and an upper case letter represents the full-scale prototype.

The mass density (ρ), Young's elasticity modulus (E), and Poisson's ratio (ν) must be identical. The geometrical scaling factor β is defined as the ratio

between a typical length dimension of the small-scale model and the full-scale prototype:

$$\beta = \frac{l}{L} \quad (3)$$

Consequently, any length dimension in the small-scale model is multiplied by the scaling factor. The other parameters are:

- Geometrical dimensions are proportional to the scaling factor: $l = \beta \cdot L$.
- Strains remains the same: $\varepsilon = E$.
- Stresses remains the same: $\sigma = \Sigma$.
- External pressures remains the same, and act at scaled locations: $p = P$.
- Disturbances propagate in the material with the same speed: $c = C$.
- Time is proportional to the scaling factor: $t = \beta \cdot T$.
- Velocities in the structures remain the same: $v = V$.

There are a number of phenomena that do not follow the scaling laws, and thus cannot be used when comparing scaled-down cases. The first phenomenon is gravitational force, which cannot be scaled experimentally according to the scaling laws. However, when dealing with a dynamic case that involves high accelerations (for example blast loading), the gravitational forces can often be neglected. Another phenomenon that cannot be scaled is material strain-rate sensitivity. Strain-rate in a small-scale model is larger than in the prototype by $1/\beta$, and thus the stresses in the full-scale prototype and the small-scale model are no longer identical. In order to overcome this, one must choose a material that is not strain-rate sensitive at least for a first extent. The last phenomenon that cannot be scaled is fracture toughness. Fracture toughness is dependent on both stress and crack length, and has units of the form $pressure \cdot \sqrt{length}$. Thus the fracture toughness of a model must be equal to $\beta^{1/2}$ times that in a prototype and that is normally physically impossible. Consequently, a failure criterion in a scaling problem cannot be fracture-mechanics based. An alternative failure criterion must be used, and this is the key issue addressed in this paper.

Remembering the external pressures must be similar, we will first examine a blast scaling problem. The most common scaling method is known as the Hopkinson (or cube root) scaling law, as found e.g. in Baker [13]. This law determines that two blast waves that are similar, are produced at the same scaled distance if the charges are the same explosive, similar in geometry, but scaled in geometric size (thus weight). For air explosions the Hopkinson scaled parameters are:

$$Z = \frac{R}{E^{1/3}}, \quad \tau^* = \frac{\tau}{E^{1/3}}, \quad \zeta = \frac{I}{E^{1/3}} \quad (4)$$

where Z is the scaled distance, τ^* is the characteristic scaled time of the blast wave, ζ is the scaled impulse, R is the distance from the center of the blast source and E is the source blast energy (E may also be replaced by W which is the weight of the explosive).

This scaling law determines that the peak pressure and velocity are similar in regard to scaling. This means that for the same value of the scaled distance Z , these quantities will remain constant. Remembering the geometrical scaling laws, where geometrical dimensions are scaled by the scaling factor β , one finds that the weight of the explosive material must also be scaled in order for the scaled distance Z to be preserved. This means that the weight of the explosive for the model is the prototype weight multiplied by β^3 .

To summarize the main points of the scaling theory of relevance to this work:

- Linear dimensions and time are multiplied by β in a small-scale model.
- The explosive weight in a small-scale model is multiplied by β^3 .
- The scaled distance Z must be identical in the small-scale model.
- The peak pressure at the scaled distance Z will be equal in the model to full scale, but the time will be reduced by β .
- Strain-rate sensitivity of the material can't be scaled, and therefore must be negligible at least for a first approximation.
- The failure criterion used cannot be fracture-mechanics (fracture toughness) based.

The above-mentioned scaling concepts have been successfully applied to close range, large scale explosions, by Neuberger et al. [14][15][16]. However, those works considered only the *structural response* of the blast-loaded plate without addressing potential fracture failure, which as discussed above was considered as non-scalable and therefore beyond the scope of that research. The goal of the present paper is to present and validate a simple alternative approach based on scalable failure criteria. This approach should therefore complement the overall blast-scaling approach, thus providing a simple, yet efficient, engineering design tool.

The paper is organized as follows: We first present the 2 failure criteria used throughout this work. Next the essential components of the numerical model are described. This section is followed by a presentation of the numerical results, showing the feasibility of the scaled failure criterion, along with the relevant numerical considerations to devise an optimal model (mesh scaling considerations). A discussion of the main results obtained for a close-range blast loading and the ballistic penetration of a plates follows, together with a concluding section.

3. Failure Criteria

3.1 Adiabatic Shear

As alluded to previously, Rittel et al. [4] suggested that the dynamic failure energy could be viewed as a failure criterion when adiabatic shear is considered. This criterion was successfully implemented by Dolinski et al. [17]. In this work, the criterion was embedded into the commercial finite element code ABAQUS [18] and tested by numerical simulation of four typical high-rate experiments: dynamic torsion test of a tubular specimen, the failure mode transition in mode II fracture of an edge crack in plain strain, and dynamic shear localization under high rate compression of a cylindrical and a shear compression specimen. A very good agreement was reported both qualitatively and quantitatively in terms of failure path selection and local strains, temperatures and critical impact velocity.

We will adopt the same point of view here, namely that there exists a critical value of the dynamic strain energy density, whose expression is given in equation (5), which dictates the onset of adiabatic shear failure. This parameter has been shown to be strain-rate independent by Osovski et al. [19]. However, it differs for each material and must be determined experimentally.

The strain energy density criterion suggests that the strain energy density is the governing factor for ASB formation. This strain energy density can be calculated as:

$$E_n = \int \sigma_{ij} d\epsilon_{ij} \quad (5)$$

This criterion was suggested by Rittel et al. [4], and was numerically modeled by Dolinski et al. [17]. The failure criterion that we here use is analogous to that used by Dolinski et al. [17]. Namely, the material starts to accumulate damage when the strain energy density reaches a critical level, $E_n = E_{n_{crit}}$.

The material loses its strength after this strain critical energy density level, until final failure when the strain energy density reaches $E_n = E_{n_{frac}}$. A new parameter called Dmg was defined for modeling of the damage evolution.

$$Dmg = \frac{E_n - E_{n_{crit}}}{E_{n_{frac}} - E_{n_{crit}}} \quad (6)$$

The stress in the material is damage dependent, by the following relation:

$$\tilde{\sigma} = \sigma \left(1 - Dmg^b\right) \quad (7)$$

Where $\tilde{\sigma}$ is the stress after enduring damage of Dmg . The parameter b is an exponent, and for our material, AM50, $b = 1$, which means a linear relationship. When an element reaches a damage value of 1, it can no longer bear stress and thus fails. This criterion is at first motivated by physical considerations (threshold energy), with a phenomenological continuation (damage). Figure 1 of Dolinski et al. [17] shows a stress-strain curve with the

critical and fracture strain energy densities. Table 1 describes the stress as a function of the strain energy density.

Three parameters define the failure: $E_{n_{crit}}, E_{n_{frac}}, b$.

The critical strain energy density $E_{n_{crit}}$ is calculated from the stress-strain curve of the material. It is the area under the curve until the onset of failure (peak stress). The parameters $E_{n_{frac}}, b$ are fit by trial and error to the experimental curve. Assuming first that $b = 1$, we gradually increase the ratio $1 < E_{n_{frac}} / E_{n_{crit}} < 4$ until we get a good fit with the experimental curve. If we do not get a good fit for $E_{n_{frac}} / E_{n_{crit}} = 4$, we leave $E_{n_{frac}}$ at its final value and start to gradually increase b until we obtain a good fit.

The parameters for the material of this study, cast aluminum-magnesium alloy AM50, are as follows [17]:

$$E_{n_{crit}} = 50[MJ / m^3]; \quad E_{n_{frac}} = 120[MJ / m^3]; \quad b = 1$$

Concerning scaling, we know that the stress and strain are equal in a small-scale and full-scale prototype. Thus, the dynamic deformation energy is equal in a small-scale model and full-scale prototype, and *this strain energy density criterion meets the requirements of scaling, under the conditions mentioned in the section on scaling laws* (a material that is not strain-rate sensitive).

3.2 Maximum Principal Stress

The second failure criterion used in this study is the maximum principal stress criterion. This criterion is used due to the fact that we don't know if blast failure will only induce a sole ASB failure mechanism. Thus, we will also use a failure criterion based on the maximum principal stress. This criterion states that failure occurs when a maximum principal stress developed in an element is greater than the ultimate tensile stress (UTS) of the material. This criterion (normal stress) is “traditionally” thought of as a brittle fracture criterion, even if this is mitigated by the fact that the UTS is considered, therefore implying a finite amount of plastic deformation prior to failure. In this work, we will not discuss the brittle vs. ductile nature of the associated failure mechanism,

keeping in mind we essentially aim at representing the creation of new surfaces (fragmentation). Since this criterion is based only on the maximum principal stress, we conclude that it *undergoes scaling* with the same conditions as the other criterion, when the material is not significantly strain-rate sensitive. Note that a strain-based criterion could alternatively be used, the latter being scalable as well.

4. Implementation of the Failure Criteria

Both criteria were implemented in the finite element software ABAQUS using a user subroutine (VUSDFLD) [17]. The user subroutine is three dimensional and includes both failure criteria. As mentioned in section 3, this user subroutine was tested and validated by Dolinski et al. [17] for a number of different cases. The conclusions were that the subroutine and failure criterion both give the expected results for the start and development of an ASB failure.

5. Numerical Simulations

5.1 Numerical Model

All of the test simulations are of circular plates that undergo an air blast of a spherical charge, using the built-in option of ConWep [12] implemented in Abaqus 6.10 [18].

We considered 4 plates marked 41, 42, 51 and 52.

Plate 41 is a full scale plate with a radius of 0.05 [m] and a thickness of 0.005 [m]. Plate 42 is also a full scale plate with a radius of 0.05 [m], but with a thickness of 0.0025 [m].

The small-scale plate for plate 41 is marked plate 51, and it is scaled by a geometrical scaling factor $\beta = 0.625$. Likewise for plate 52 with respect to plate 42.

The complete data for all of the plates are given in Table 2, where Z is the scaled distance according to Hopkinson cube root scaling laws.

The periphery of the plate is clamped in all directions. The plate itself was always positioned so that the center of the bottom base of the plate was at (0,0,0), while the charge was placed at (0,0,Ref Point), listed in Table 2, facing the upper base of the plate.

For all plates, three meshes (coarse, medium and fine) were generated with hexahedral elements of type C3D8R, as explained below.

Since all geometrical properties undergo scaling, the global element size is also scaled according to the scaling laws. Consequently, for plates 41 (full-size) and 51 (41-scaled) the global element size in the *fine* mesh was ~0.39 [mm] and ~0.24 [mm] respectively. The fine mesh comprises 801,000 elements.

For plates 42 (full-size) and 52 (42-scaled) the global element size in the *medium* mesh was ~0.39 [mm] and ~0.24 [mm] respectively. The medium mesh comprises 370,000 elements.

For plates 42 (full-size) and 52 (42-scaled) the global element size in the *coarse* mesh was ~0.5 [mm] and ~0.31 [mm] respectively. The coarse mesh comprises 195,000 elements.

All global element sizes and the number of elements for all of the plates are presented in Table 3.

It is noted here that even though the global element size was scaled according to the scaling laws, the mesh itself isn't identical in terms of element shapes and locations. The mesh itself depends on where the mesh starts from, the meshing method and other factors that cannot always be controlled. The mesh itself does not have to be identical in order to obtain accurate results.

The material of the plates is AM50. This material was previously characterized [20] so that all its dynamic mechanical characteristics are well documented. The material properties of AM50, including the parameters for the Johnson-

Cook constitutive model [21], are presented in Table 4. This model is described by:

$$\sigma = \left[A + B(\varepsilon_p)^n \right] \left(1 + C \ln \frac{\dot{\varepsilon}}{\dot{\varepsilon}_0} \right) \left[1 - \left(\frac{T - T_0}{T_m - T_0} \right)^m \right] \quad (8)$$

where A, B, C, m, n are material parameters, ε_p is the plastic strain, $\dot{\varepsilon}$ is the strain-rate, $\dot{\varepsilon}_0$ is the reference strain-rate, T_0 is the initial temperature and T_m is the melting temperature. The data in Table 4 was taken from the work done by Dolinski et al. [17], who derived the material parameters from work done by Wang and Rittel [20],[22].

The user subroutine does not accept the JC equation as an input, and therefore stress-strain curves were generated using equation (8) for a number of temperatures and strain-rates.

Figure 2 shows the stress-strain curves for strain-rates of 1, 3500 and 10000 1/s. Remembering from section 2 that the strain-rate in a small-scale model is divided by the scaling factor, in this case the strain-rate in the small-scale model is multiplied by 1.6. As shown in Figure 2, the difference in flow stress between the curves in the dynamic regime is relatively minor.

5.2 Numerical results

5.2.1 Mesh sensitivity and convergence

The first case we discuss is the case with plate 41, the full-size plate, and plate 51, the scaled plate.

Simulations were conducted for each plate with each mentioned mesh (fine, medium and coarse). The fracture pattern of plate 41 is shown in Figure 3.

When comparing the different meshes of plate 41 we note the two following points:

1. The stress distribution grows increasingly constant as the mesh is refined.
2. The crack's length reaches a finite value as the mesh is refined.

Convergence in this work is to be understood as based on the distribution and value of the Mises equivalent stress, and the nature of the pattern of cracks

representing failure. Therefore, both of these points show that convergence is reached at 391k elements, the medium mesh. As each test case converges, the stress distribution similarity and the scaling similarity improve.

In terms of convergence of plate 51, the scaled plate, is similar to plate 41, and therefore we will not discuss it in detail.

The second case to be addressed is that of plates 42 (full-size) and 52(scaled plate). The fracture pattern for all mentioned meshes (fine, medium and coarse) of plate 42 is shown in Figure 4. Here, the plates formed a distinct dish as the main failure mode.

When comparing the different meshes of plate 42 we note the two following points:

1. The stress distribution grows increasingly similar as the mesh is refined.
2. The dish's radius reaches a finite value as the mesh is refined.

Both of these points show that convergence is reached at 370k elements, the medium mesh. As each test case converges, the stress distribution similarity, and therefore the scaling, improve.

Figure 5 shows the displacement of the central point of the plate (0, 0, 0) as a function of the time for different meshes of plate 42. From this figure, one can see that the displacement of the central point of the plate is almost identical. The maximum normalized difference between adjacent curves is 0.5%. The first data point ($t = 9 \cdot 10^{-5} [s]$) on the curve is the onset of failure and cracking of the plate, marked by a black arrow. The second point ($t = 1.35 \cdot 10^{-4} [s]$), marked by a red arrow corresponds to the full disconnection of the dish from the plate. The times are identical for all of the meshes.

Again, in terms of convergence of plate 52 vs. 42, one observes similar results so that this case will not be further discussed here.

5.2.2 *Scaling of the problem*

Figure 6 shows the Von Mises stress of the *fine* mesh of plates 41 (full-size) and 51 (scaled).

In terms of scaling, it is evident from Figure 6 that the normalized radius of the cracks is similar, and so is the stress distribution. The stress is not exactly identical between the two plates because there is a mild dependence of the stress on strain-rate or mesh geometry (see section 5.1), but as one can see, this does not significantly affect the scaling. It is thus concluded that scaling is successfully obtained for these two plates.

Figure 7 shows the Von Mises stress of the *medium* mesh of plates 42 (full-size) and 52 (scaled). One can see that we obtain scaling as the radius of the dish is similar, and so is the stress distribution. Again the stress isn't exactly constant due to the above mentioned mild strain-rate sensitivity or mesh geometry. It is therefore concluded that scaling is obtained for these two plates as well.

Figure 8 shows the scaled displacement at the center of the plate (0, 0, 0) as a function of the scaled time for plates 42 and 52. This figure was created using the known geometrical scaling relations mentioned in section 2. First, the displacement of the small-scale model is divided by the geometrical scaling factor. Next, the time scale of the small-scale model is divided by the geometrical scaling factor.

5.3 Plate Failure

In all of the test cases (41, 42, 51, 52), failure was caused by the maximum principal stress criterion. This observation comes from the fact that the damage parameter in the failed elements remained equal to zero. The failure mechanism in these cases is not ASB governed. In spite of that, one can perform an additional verification of scaling for this criterion. To do so, one considers the total strain energy density in the full size case and compares it to that of the scaled case. The user subroutine calculates this strain energy density, and uses it to determine the damage parameter.

Figure 9 presents the distribution of the strain energy density in plate 42, the full-scale plate, and plate 52, the small-scale plate.

It is evident from Figure 9 that this strain energy density is indeed identical for both cases. Note that originally, the limits of the contour in the legend were slightly different for the two plates. In order to check if this is misleading due to a specific element or perhaps a numerical misrepresentation near the clamped edge, we checked the same plot with user defined contour limits (Figure 9). Any elements outside of our manual limits are colored gray or black, depending if it is larger or smaller than the pre-set limits. A thorough search in the model didn't reveal almost any gray or black elements which further strengthens the point that one or a few singular elements caused the difference in automatic scale selection. Another advantage of this contour selection is that the intervals are now the same for the two cases, allowing for easy comparison.

In order to further verify that the strain energy density is indeed similar, this parameter was plotted as a function of time in the elements closest to the center of the plate (Figure 10). All of the blue lines belong to elements from case 42, the full-scale plate, while the red lines belong to elements from case 52, the small-scale plate. Figure 10 shows (again) the similarity in local strain energies for the two investigated cases. The strain energies of the elements in case 42 range between $4.91 \cdot 10^6 - 5.23 \cdot 10^6 [J/m^3]$, whereas for plate 52, the local strain energy density ranges between $5.08 \cdot 10^6 - 5.17 \cdot 10^6 [J/m^3]$. These minor differences are most likely due to the small differences we saw in stress distribution (and also in strain distribution), as previously discussed. Also, the element locations and shapes are slightly different, as the meshes are not fully identical. While the global element size is scaled, the scaled mesh is not identical to that of the full size plate. It is therefore concluded that the strain energy density (criterion) undergoes scaling.

5.4 Crack Propagation vs. Nature of the Mesh

Crack propagation in all the simulations is based on fulfillment of the failure criteria, on an element basis. When an element fails via one of the two criteria, it is deleted from the screen and does not participate in the analysis any longer. The deletion of elements "allows" cracks to propagate across the plate, as an increasing number of elements fail. In this section we address the

effect of the mesh, namely structured vs. unstructured. All of the simulations consisted of linear hexahedral elements of type C3D8R. Two different meshes were considered, for this purpose, as follows:

1. An unstructured mesh was used, that is the mesh used in all the previous sections. This mesh is a free mesh, only the global element size is dictated. The meshing method is a free one, thus the outcome is an unstructured mesh.
2. A structured radial mesh, where a small circle in the middle of the plate is meshed independently by squares. The number of elements in this case is determined by the number of elements along the radius instead of determining a global element size.

Figure 11 and Figure 12 show the results obtained for unstructured and structured mesh of plates 41 and 42, respectively.

Our previous results established convergence in the unstructured mesh for a medium mesh size, so that the following study was carried out with this kind of converged mesh. For the structured mesh we checked convergence separately. For plate 41, one can note that convergence is achieved considering the number of the main cracks, but the angles (paths) and lengths of these cracks differed between mesh sizes. The cracks were straight in all of the structured meshes. For plate 42 (Figure 12), convergence is achieved considering the radius of the plug, whereas the minor cracks in the middle and in the outer part of the plate differ in location. Moreover, for the structured mesh the cracks are propagating in a rectilinear mode only.

Those results show that the unstructured mesh looks much more realistic in terms of crack propagation and failure, as it is not constraining the crack propagation path as the structured mesh does. The cracks in the structured mesh are too straight to look realistic. Also, when zooming in (Figure 13), we see that the border between the radial mesh and the independent square mesh in the middle of the plate was cracked almost perfectly in both cases.

From Figure 11 and Figure 12, it can be concluded that the unstructured mesh provides more realistic crack patterns, of a kind that one would observe experimentally [8], when the failure mechanism is not due to shear as in our case [8].

5.5 Penetration Simulations

When conducting the blast simulations, we noted that the plates did not fail due to the strain energy density criterion. For the purpose of showing that the failure criterion successfully predicts and scales ASB failure, we simulated one of the experiments conducted by Borvik et al. [23]. The rationale for this simulation is that adiabatic shear is one of the most common failure modes in this kind of experiments. The experiment itself consists of a clamped plate impacted with a blunt-nosed cylindrical projectile. The plate is square, but it is clamped in a rigid frame with an inner clamp diameter of 500 mm, so when modeling this problem we model the plate as a circular clamped plate. The plate is made from Weldox 460 E, and the projectile from Arne tool steel. The material properties of both plate and projectile can be found in [23][24]. The thickness of the plate is 12 mm, and the projectiles have a nominal mass, diameter and length of 197 g, 20 mm and 80 mm, respectively. Using the material properties and the graphs in [23][24], we obtained the value for $E_{n_{crit}}$, and determined $E_{n_{frac}}$ numerically. The values are as follows:

$$E_{n_{crit}} = 450[MJ / m^3]; E_{n_{frac}} = 750[MJ / m^3]; \quad b = 1$$

We note here that since the failure method in this simulation is known to be ASB, we only used the strain energy density criterion. When using both criteria, the simulations predicted early failure through the UTS criterion, which was not observed in the experiments. This is an issue to be further looked into in further studies.

The damage value that was determined as the failure of an element is 0.3, as in [23]. The experiment we modeled is labeled #1 in [23], where the velocity of the projectile is 303.5 m/s.

Since the problem is symmetric, we modeled a quarter of the plate and projectile, applying the necessary symmetry conditions. For simplicity, the scaling factor β was chosen to be 0.5 in this case.

Figure 14 shows the full-scale case and the small-scale case, and it clearly shows that the shape of the plug is similar for both cases. Figure 14 also shows that the residual velocity of the plug and projectile are similar for both cases.

In the original article the reported residual velocities were 199.7 m/s for the projectile, and 242.3 m/s for the plug. In the simulations the residual velocity of the projectile was 203.5 m/s, and 247.4 m/s for the plug. These results are quite close to the original experimental results.

This simulation shows that the strain energy density failure criterion undergoes scaling, and can successfully predict failure by ASB formation.

6. Discussion and Conclusions

In this study we show that scaling dynamic failure is possible when using two competing criteria, namely: maximum normal stress to describe separation (cracking) and a strain energy density-based criterion that describes adiabatic shear failure. Those criteria are used as an alternative to fracture mechanics considerations which, because of the inherent length scale, cannot undergo scaling, therefore cannot be implemented in simulations of dynamic failure situations.

In this work, in addition to paying attention to proper geometrical scaling of the problem and cube root scaling of the explosive charge, this study shows that the mesh itself must be scaled. An ideal situation would require the mesh to remain self-similar which was not exactly the case in the present simulations. However, the degree of resemblance between the full scale and scaled problems was sufficiently high to warrant that scaling was successfully passed. Two kinds of meshes were compared, namely structured and unstructured. The results differed between the two kinds of meshes. It was concluded that the unstructured mesh is much less constraining in terms of crack path so that it should be used. It is obvious that the true validation will only come from experiments. Another issue that was addressed in this work is that of the convergence of the calculations. Numerical convergence is usually quantified as a norm of a calculated result vs. e.g. an analytical one. In that case, there is no available analytical result to compare to, and convergence was verified with respect to the number of cracks, their path, the plug size and the stresses in the plate. Convergence was deemed to be fulfilled once those parameters showed no significant sensitivity to further refinement of the mesh.

Two failure criteria were used in this work: attainment of a critical strain energy density level in the element and a maximum normal stress value. It was shown that each criterion undergoes scaling, and as such are valuable candidates to simulate failure in dynamic loading considerations. While the first criterion has a clear physical origin, the second is generally applied to brittle fracture, which is not exactly the case in our simulations. One could definitely think of a more physical strain-based criterion for example, but the use of the present UTS criterion just comes to replicate the creation of new fracture surfaces.

In this context, two specific kinds of simulations were carried out. The first one is that of a plate subjected to an explosion from close range. In this case, the dominant active failure criterion is the UTS (maximum normal stress) one, with some shearing acting on the clamped periphery of the plate. Therefore, to see the operation of the strain energy density criterion, we simulated a reported experimental case of ballistic penetration. The two kinds of simulations showed convincingly that the failure criteria do indeed undergo scaling and provide a meaningful insight. Of course, as mentioned before, the ultimate validation must be experimental, but it is deemed that the current results do provide useful guidelines as to how to model and predict failure of a small scale model, just as was done for structural response of the blast loaded plates by Neuberger et al. [14].

The fact that for the ballistic penetration, the joint application of the two failure criteria yielded unrealistic results of early fracture just indicates that the UTS criterion was not ideal in this case, either as a criterion in itself or through the values of the material parameters. We deliberately decided not to modify those parameters until the desired results would be obtained (no early cracking) in order to stay in line with the values reported in the experimental work of Borvik et al. [23]. Future work will have to come to terms with the exact values of the material properties and also regarding the choice of a more adequate failure criterion that describes ductile tearing. All in all, the present study provides an illustration of a viable alternative to fracture-mechanics or damage-based failure criteria which do undergo scaling while remaining simple to implement in engineering calculations.

The conclusions from the study are:

- Maximum stress and strain energy density criteria both undergo successful scaling. Those criteria are scalable examples of alternatives to fracture-mechanics based criteria.
- Adiabatic shear is well described by the strain energy density criterion while creation of fracture surfaces is reasonably well reproduced by the maximum stress criterion.
- Dynamic failure, be it due to explosive loading or ballistic penetration, is scalable and can be modeled numerically.
- Future research should be invested into the experimental validation of the present numerical results.

Acknowledgement: Drs. E. Kochavi and A. Dorogoy are kindly acknowledged for useful discussions and assistance throughout this research work.

References

- [1] N. Jones, "Structural Impact". (Cambridge University Press, 1989).
- [2] Y. Bai, B. Dodd, "Shear localization: occurrence, theories, and applications", (Oxford: Pergamon), 1992.
- [3] C. Zener, J.H. Hollomon, "Effect of strain rate upon plastic flow of steel", 1944, J. Appl. Phys. 15, 22–32.
- [4] D. Rittel, Z.G. Wang and M. Merzer, "Adiabatic shear failure and dynamic stored energy of cold work", (2006), Phys. Rev. Letters, Vol 96(7), 075502-1-075502-4.
- [5] M. G. Cockcroft and D. J. Latham, "Ductility and the workability of metals", (1968) Journal of the Institute of Metals, 96, 33–39.
- [6] Z.L. Zhang, C. Thaulow, J. Odegard, "A complete Gurson model approach for ductile fracture", 2000, Engineering Fracture Mechanics, 67, 155-168.
- [7] M.E. Kipp and D.E. Grady, "Dynamic fracture growth and interactions in one dimension", 1985, J. Mech. Phys. Solids 33, 399–415.
- [8] P. Longère, A.-G. Geffroy-Grèze, B. Leblé and A. Dragon, "Ship structure steel plate failure under near-field air-blast loading: numerical simulations vs experiment", 2013, International Journal of Impact Engineering. 62, 88-98.
- [9] N.F. Mott, "Fragmentation of shell cases", 1947, Proceedings of the Royal Society of London, Series A (Mathematical and Physical Sciences), Vol. 189, pp. 300-308.
- [10] H. Zhang, K. Ravi-Chandar, "Dynamic fragmentation of ductile materials", (2009), J. Physics D: Applied Physics, 42, 214060.
- [11] S. Dey, T. Børvik, O.S. Hopperstad, M. Langseth, "On the influence of fracture criterion in projectile impact of steel plates", Computational Materials Science 38 (2006) 176–191.
- [12] ConWep, Conventional Weapons Effects, US Army TM-855, 1992.
- [13] W. Baker, Explosions in air, Austin: University of Texas Press; 1973.
- [14] A. Neuberger, S. Peles and D. Rittel, "Scaling the response of circular plates subjected to large and close-range spherical explosions. Part

- I: air-blast loading”, 2007, International Journal of Impact Engineering, 34, 859-873.
- [15] A. Neuberger, S. Peles and D. Rittel, “Scaling the response of circular plates subjected to large and close-range spherical explosions. Part II: buried charge”, 2007, International Journal of Impact Engineering, 34, 874-882.
- [16] A. Neuberger, S. Peles and D. Rittel, “Springback of circular clamped armor steel plates subjected to spherical air-blast loading”, 2009, International Journal of Impact Engineering, 36, 53-60.
- [17] M. Dolinski, D. Rittel, A. Dorogoy, "Modeling adiabatic shear failure from energy considerations", (2010), Journal of the Mechanics and Physics of Solids, 58, 1759-1775.
- [18] Abaqus, 2010. Finite Element Package (explicit). Dassault Systemes Providence, RI.
- [19] S. Osovski, Y. Nachmany, D. Rittel, P. Landau and A. Venkert “ On the dynamic character of localized failure ”, (2012), Scripta Materialia 67, 693-695.
- [20] D. Rittel and Z. Wang, “Thermo-mechanical aspects of adiabatic shear failure of AM50 and Ti6Al4V alloys”, (2008), Mechanics of Materials, 40, 629-635.
- [21] G.R. Johnson, W.H. Cook, "Fracture characteristics of 3 metals subjected to various strains, strain rates, temperatures and pressures", (1985), Engineering Fracture Mechanics 21 (1), 31-48.
- [22] Z. Wang, PhD thesis, "Experimental study of adiabatic shear band formation", (2007), Mechanical Engineering Dept. Technion, Haifa, p.120.
- [23] T. Børvik, M. Langseth, O.S. Hopperstad, K.A. Malo, "Ballistic penetration of steel plates", International Journal of Impact Engineering 22, 855–886, 1999.
- [24] T. Børvik, O.S. Hopperstad, T. Berstad, M. Langseth, "A computational model of viscoplasticity and ductile damage for impact and penetration", European J Mech A/Solids 2001;20:685–712.

E_n	$\tilde{\sigma}$
$E_n \leq E_{n_{crit}}$	σ
$E_{n_{crit}} \leq E_n < E_{n_{frac}}$	$\sigma(1 - Dmg^b)$
$E_n = E_{n_{frac}}$	0

Table 1: The stress as a function of the strain energy density

Plate #	41 (full-size)	51 (41-scaled)	42 (full-size)	52 (42-scaled)
Radius [m]	0.05	0.03125	0.05	0.03125
Thickness [m]	0.005	0.003125	0.0025	0.0015625
Time Step [s]	0.0003	0.0001875	0.00025	0.00015625
Ref Point [m]	0.15	0.09375	0.15	0.09375
TNT Mass [kg]	0.04	0.009765625	0.04	0.00976563
Charge Radius [m]	0.018027185	0.011266991	0.0180272	0.011266991
Dist of Exp [m]	0.145	0.090625	0.1475	0.0921875
Z	0.423982572	0.423982572	0.43129262	0.431292616
Distance/radius	8.043407585	8.043407585	8.18208703	8.182087027

Table 2: The dimensions of the plate and parameters in the simulation

	41 (full-size)	51 (41-scaled)	42 (full-size)	51 (41-scaled)
Coarse global element size [mm]	0.63	0.39	0.5	0.31
Coarse number of elements	196,000	196,000	195,000	195,000
Medium global element size [mm]	0.5	0.31	0.39	0.24
Medium number of elements	391,000	391,000	370,000	370,000
Fine global element size [mm]	0.39	0.24	0.31	0.2
Fine number of elements	801,000	801,000	781,000	781,000

Table 3: The global element size and number of elements for all the meshes of all the plates

$E [GPa]$	ν	$\rho [kg / m^3]$	$c [J / Kg \cdot K]$	$T_m [^{\circ}K]$	$T_0 [^{\circ}K]$
45	0.35	1770	1020	708	300
$A [MPa]$	$B [MPa]$	n	C	$\dot{\epsilon}_0 [s^{-1}]$	m
90	5000	1.26	0.015	1	0.88

Table 4: The material properties and JC parameters for AM50

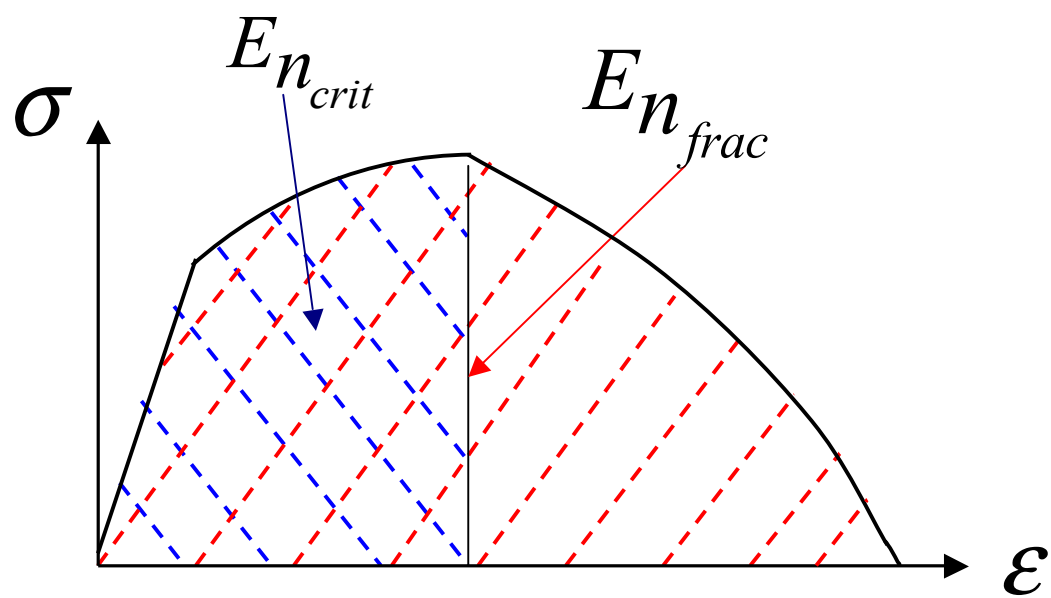


Figure 1: A schematic stress-strain curve that shows the strain energy density failure criterion

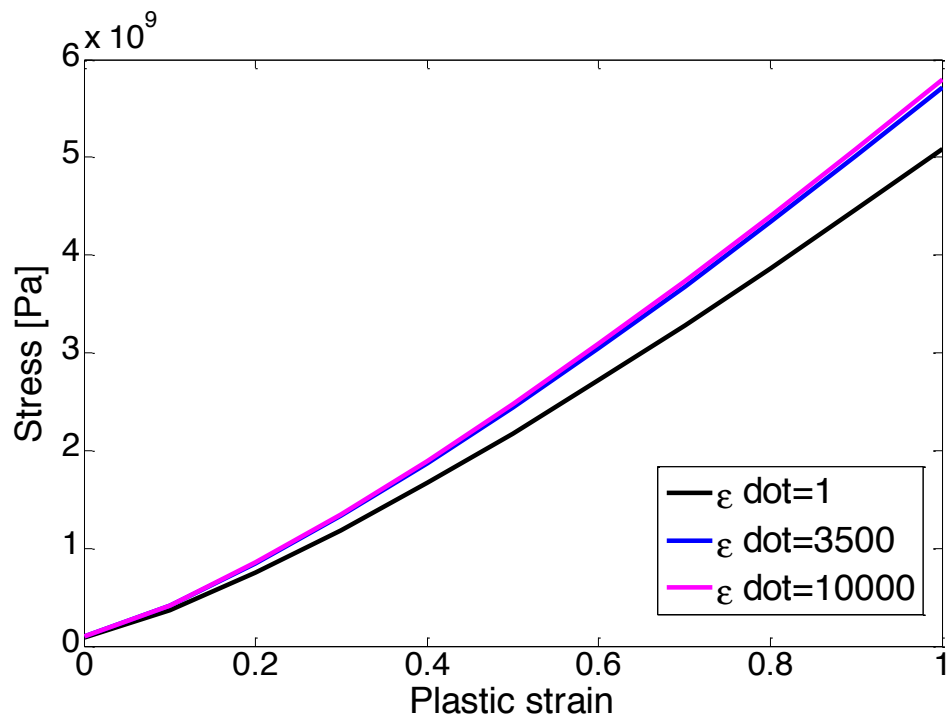


Figure 2: Stress-strain curves for AM50 at strain-rates of 0, 3500 and 10000 [1/s]

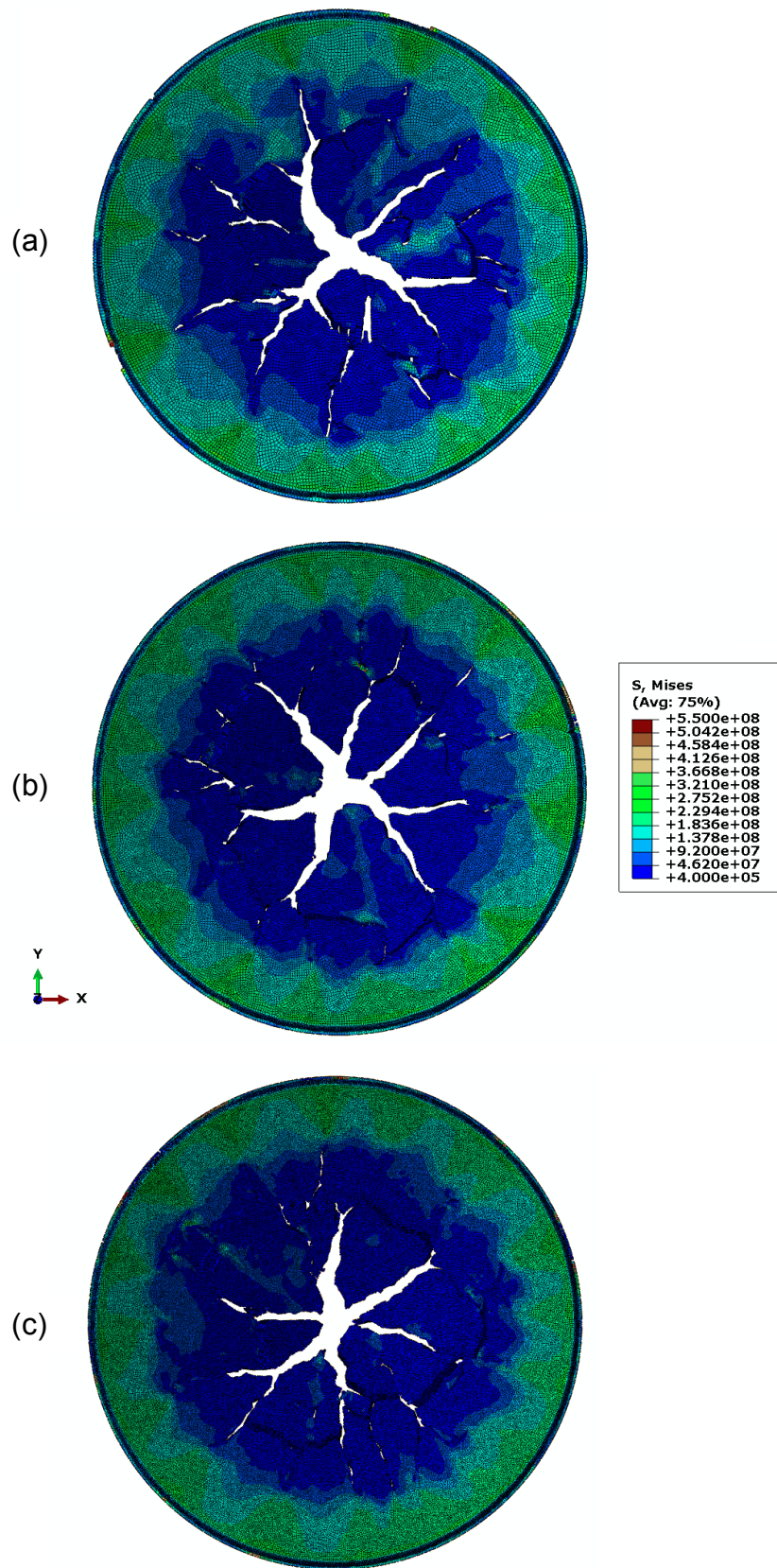


Figure 3: The three meshes of plate 41. (a) coarse; (b) medium; (c) fine

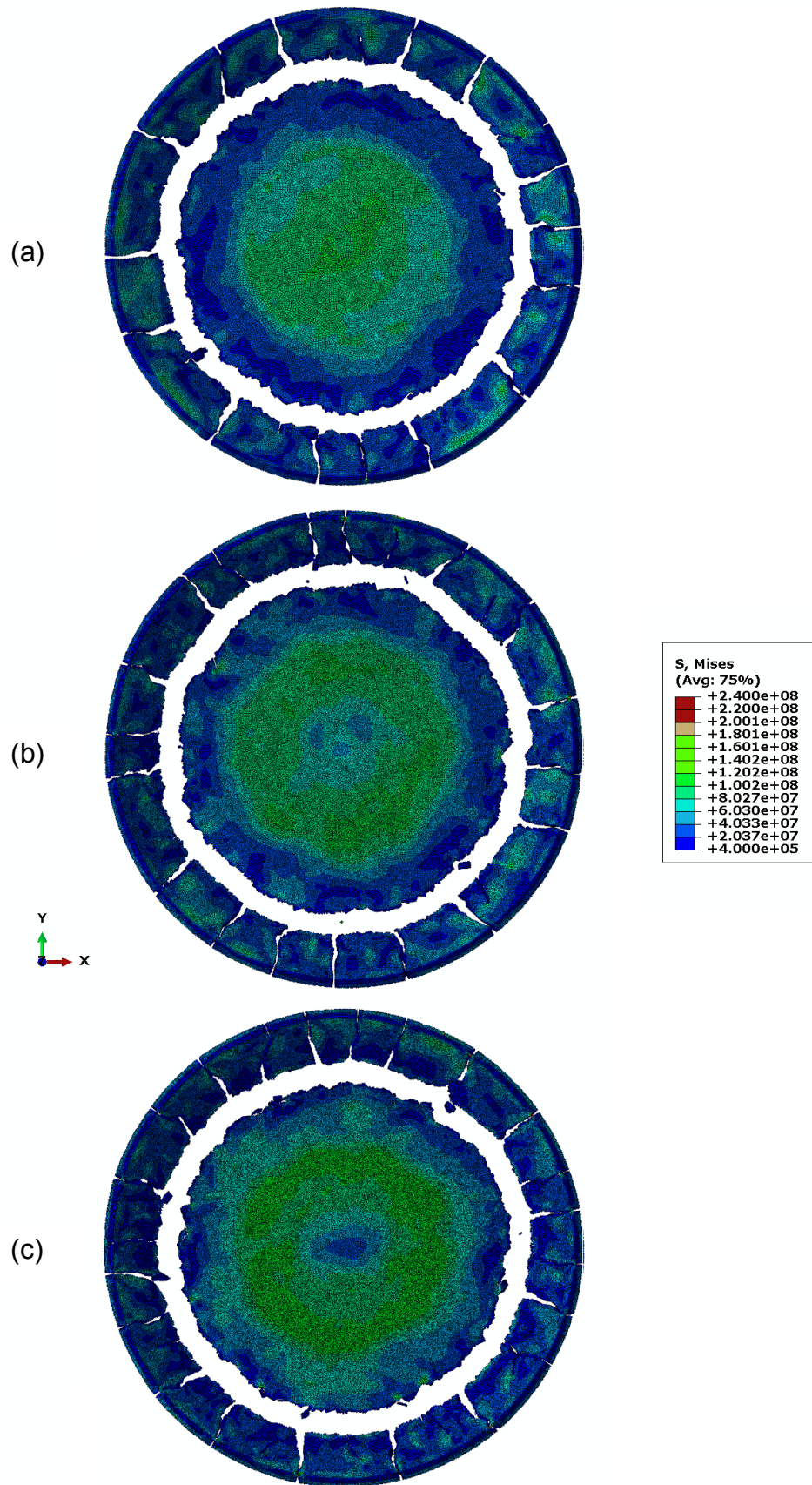


Figure 4: The three meshes of plate 42. (a) coarse; (b) medium; (c) fine

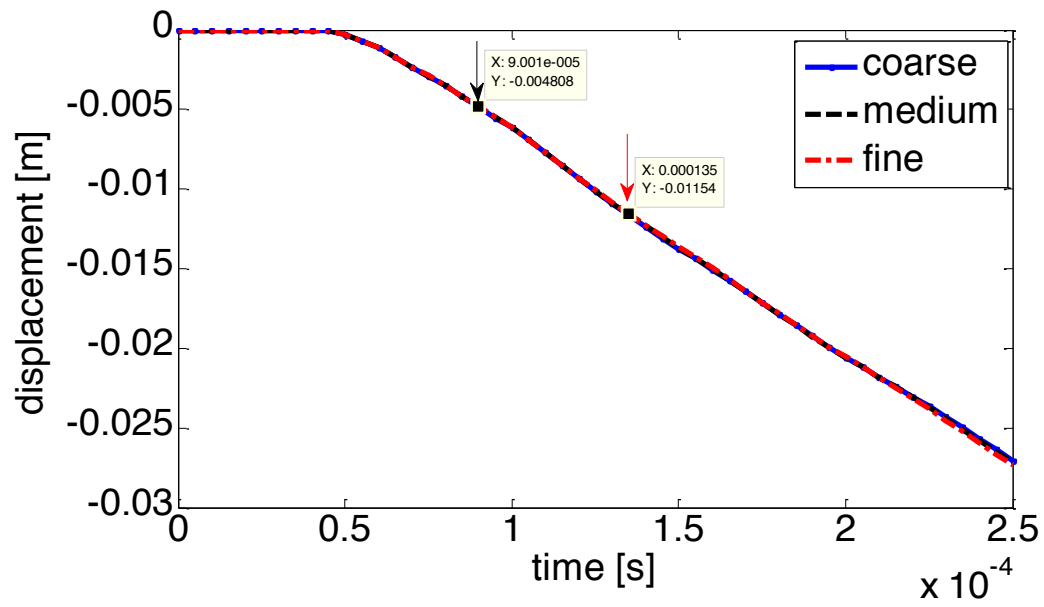


Figure 5: The displacement of the central point of the plate (0, 0, 0) as a function of the time in the different meshes of plate 42.

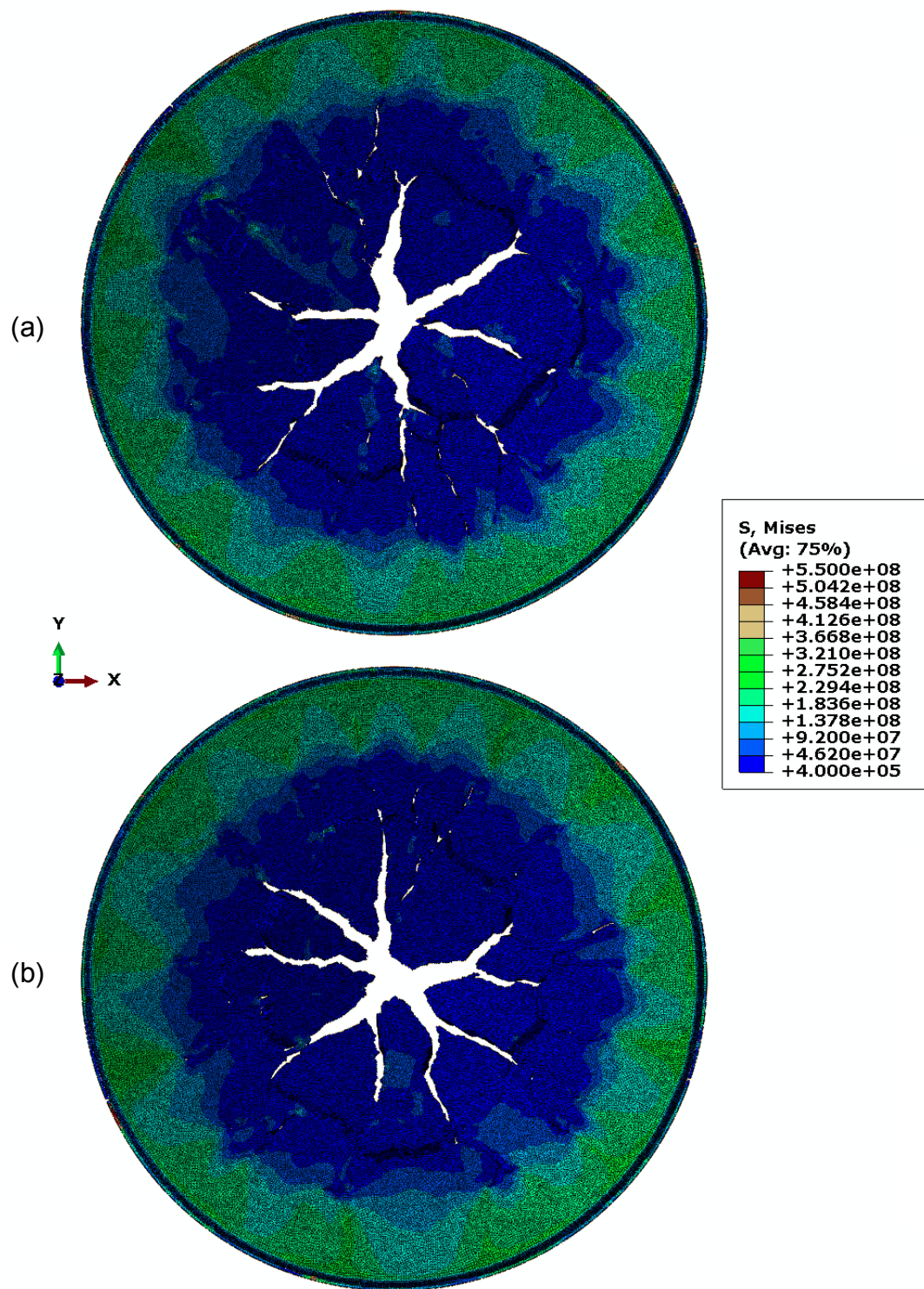


Figure 6: Von Mises stress of (a) Plate 41(full-size); (b) Plate 51(scaled)

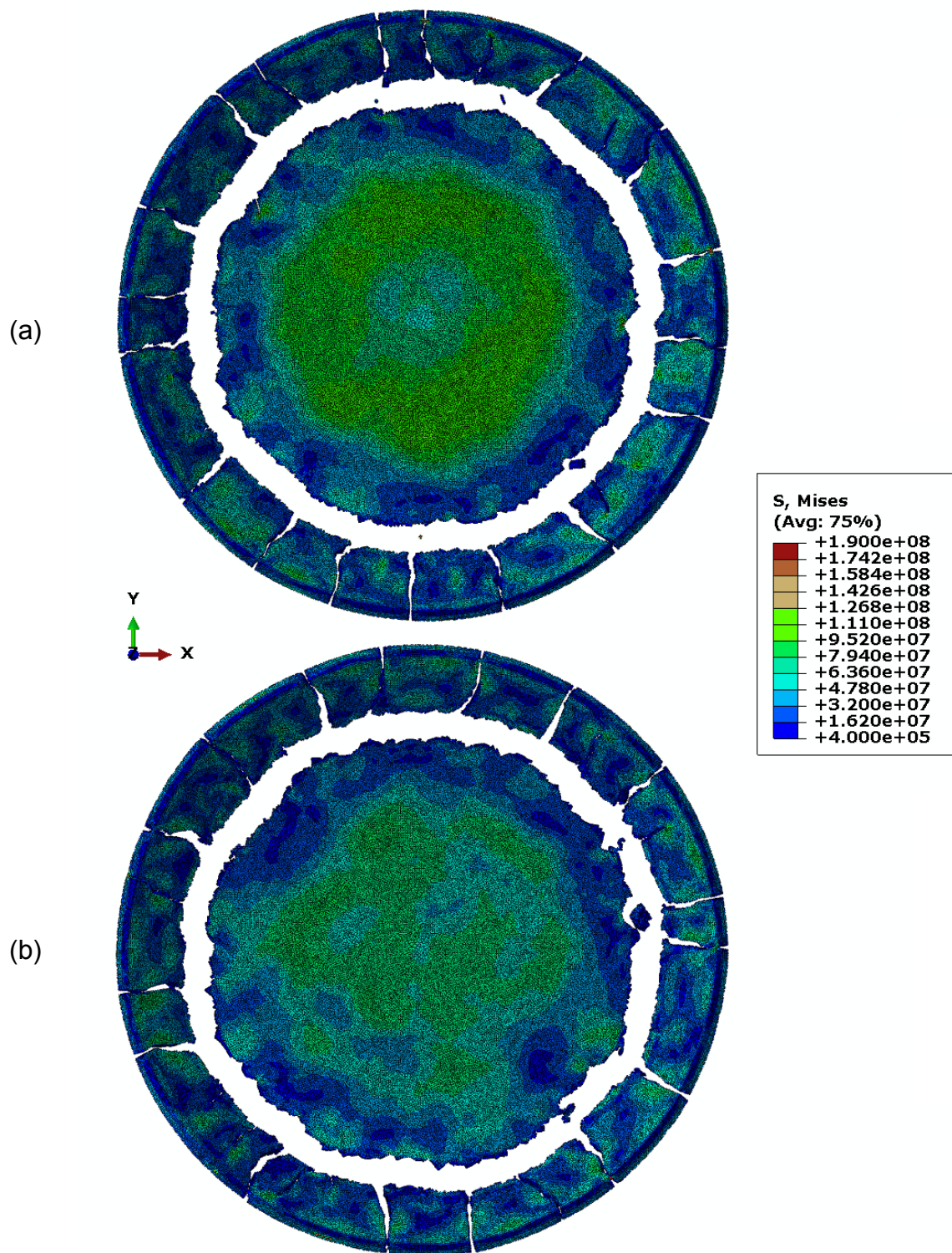


Figure 7: Von Mises stress of (a) Plate 42(full-size); (b) Plate 52(scaled)

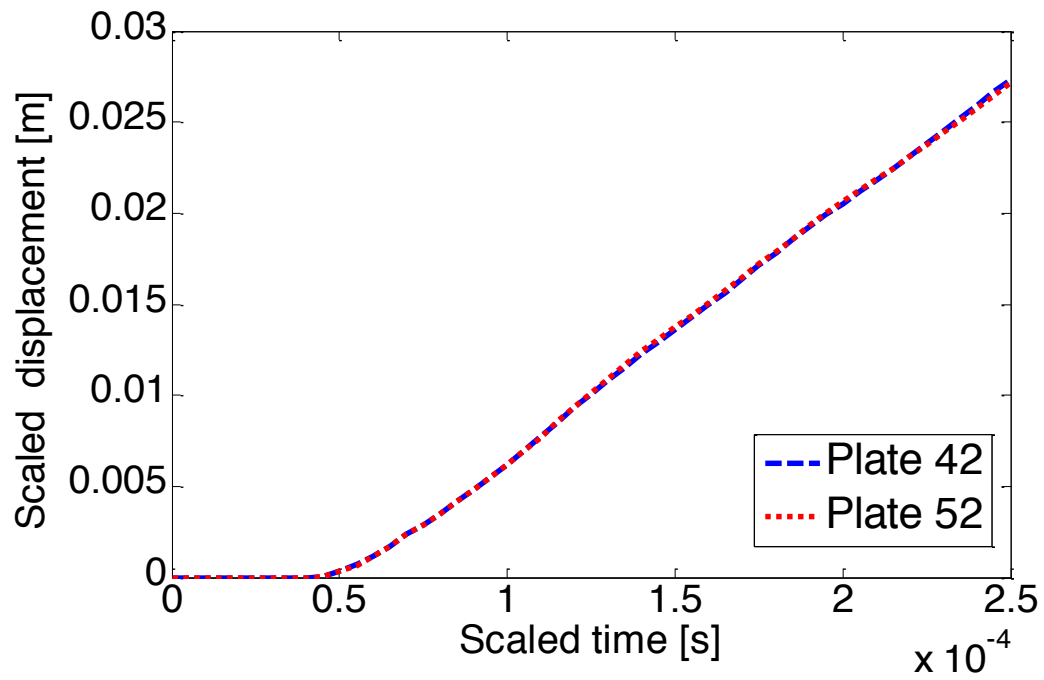


Figure 8: The normalized displacement as a function of the scaled time in plates 42 and 52.

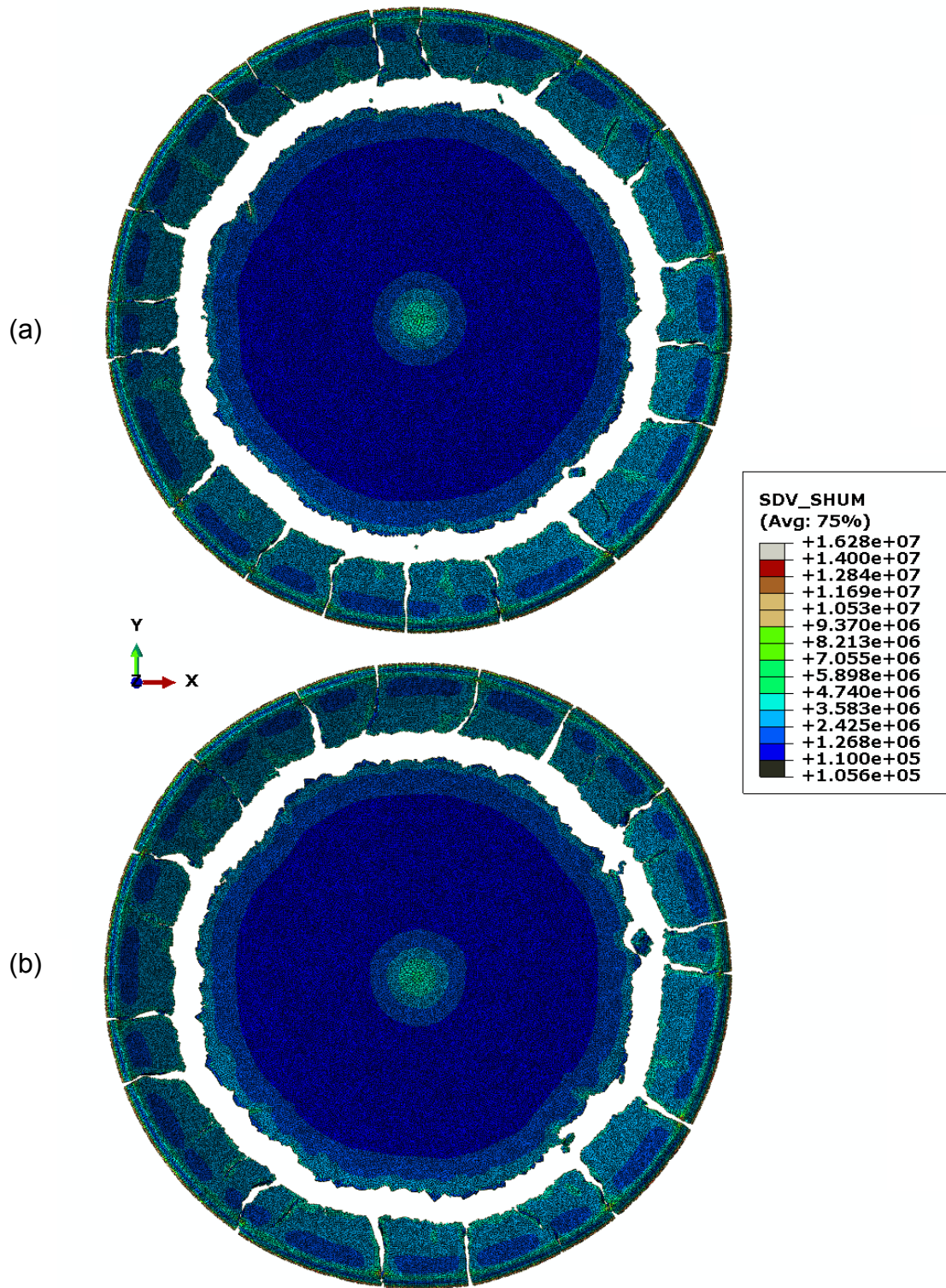


Figure 9: The distribution of strain energy density in plates (a) 42 (full size) and (b) 52 (scaled).

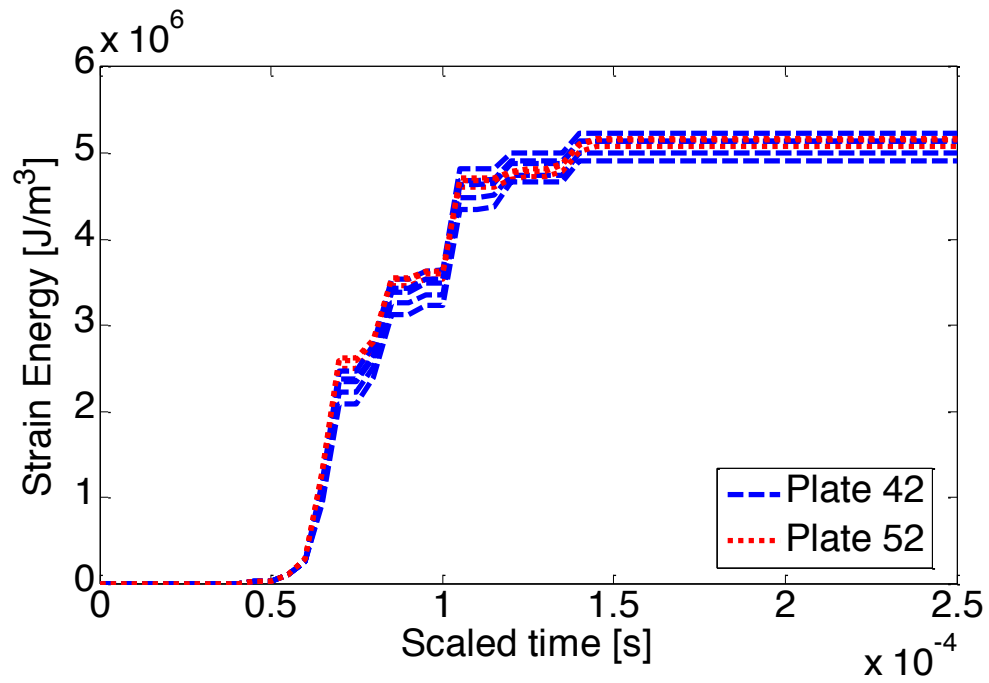


Figure 10: The strain energy density versus the time in the elements that share the middle node of the plate in plates 42 and 52.

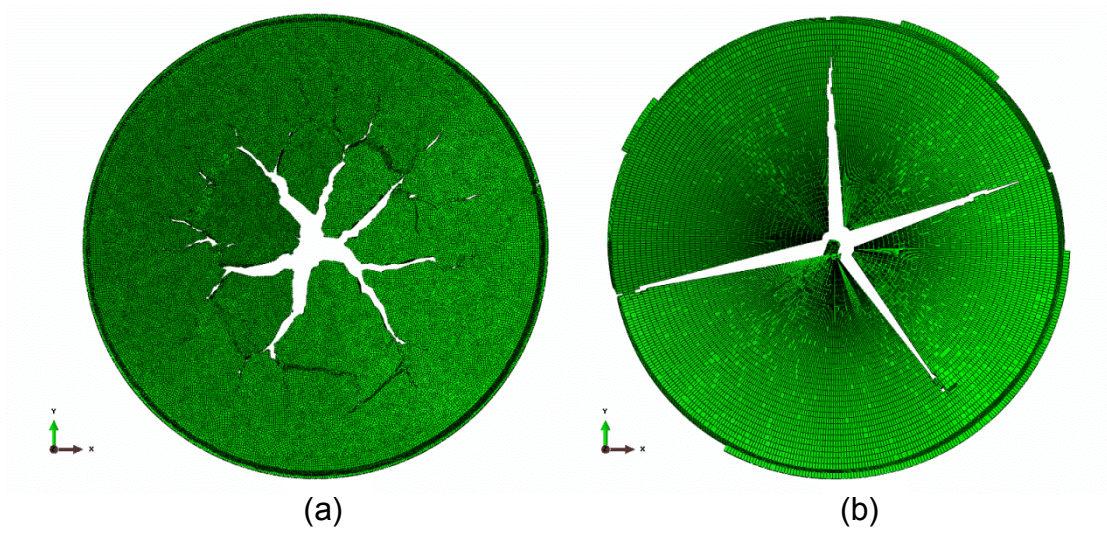


Figure 11: The different meshes of plate 41. (a) Unstructured. (b) Structured

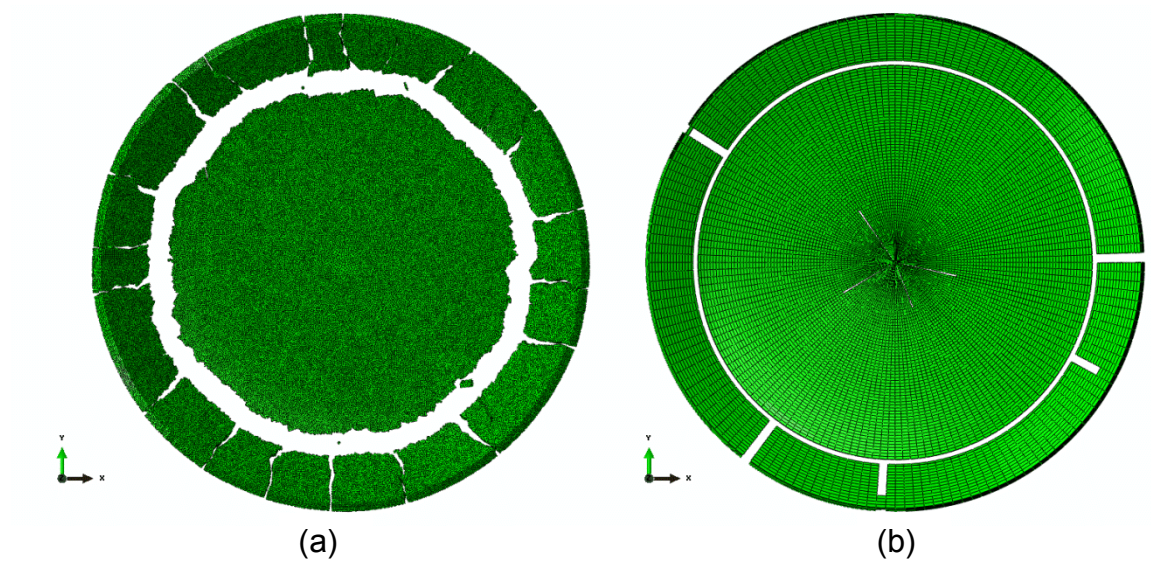
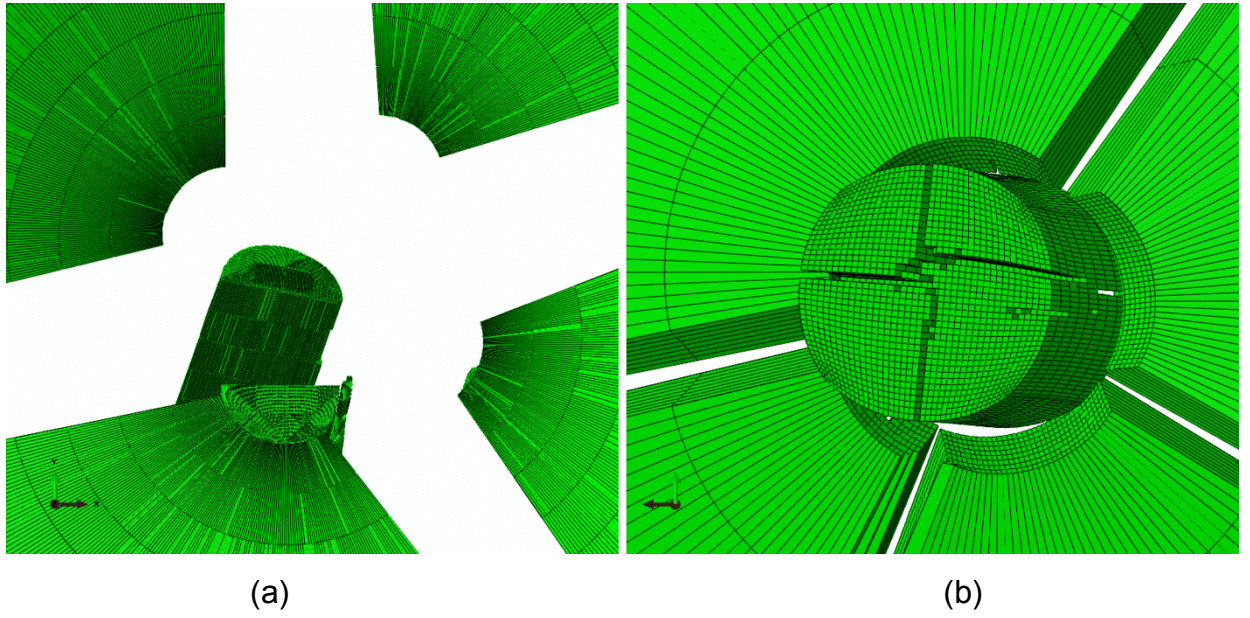


Figure 12: The different meshes of plate 42. (a) Unstructured. (b) Structured.



**Figure 13: Enlargement of the center of the plate for both structured meshes.
(a) Plate 41. (b) Plate 42**

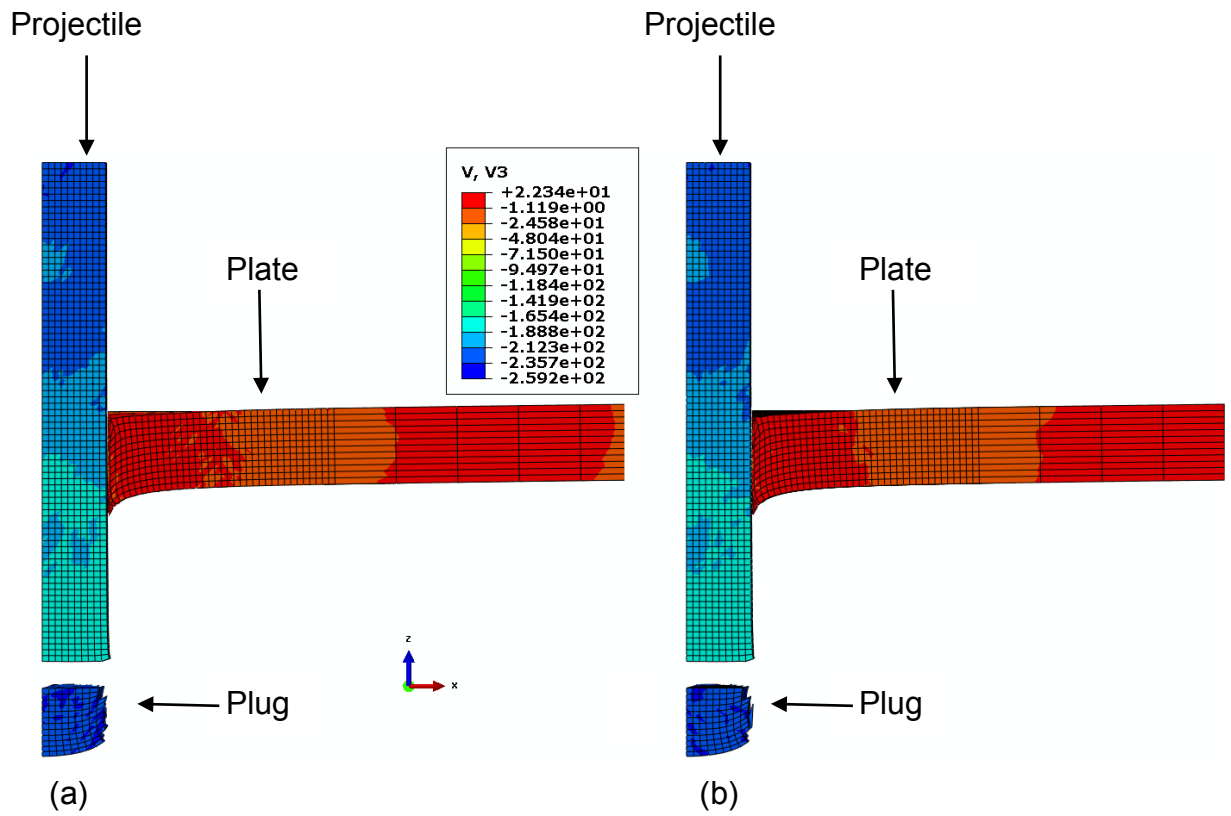


Figure 14: The velocity in the direction of the projectiles movement. (a) full-scale case (b) small-scale case